

Particle acceleration and inverse Compton emission from shear boundary layers in relativistic jets

Tej Chand* and **Markus Böttcher**

*Centre for Space Research, North-West University,
Potchefstroom, 2520, South Africa*

E-mail: chandtej11@gmail.com, Markus.Bottcher@nwu.ac.za

Powerful jets of radiation and particles emitted from the super-massive black holes residing in the centres of some active galactic nuclei (AGNs) can travel undisrupted over kpc scales. The radio and optical observations of the large-scale jets and theoretical studies from MHD simulations suggest a radially stratified structure of relativistic jets. In this scenario, a fast, low-density component of the jet flow, called the spine, is surrounded by a slow, denser plasma fluid called the sheath. The spine-sheath boundary layers formed in the relativistic jets of AGNs or gamma-ray bursts (GRBs) can be conducive to efficient particle acceleration. We study the self-generated magnetic field and particle acceleration in such shear boundary layers (SBLs) using 2D particle-in-cell (PiC) simulations. We also present the self-consistent calculation of the radiation spectrum produced by inverse Compton scattering of relativistic electrons in an external soft photon field.

*High Energy Astrophysics in Southern Africa 2022 - HEASA2022
28 September - 1 October 2022
Brandfort, South Africa*

*Speaker

1. Introduction

The relativistic outflows emanating from the vicinity of the black-hole event horizon over the kpc scale appear common in AGN, X-ray binary systems, and GRBs. The relativistic jets are generally anticipated to manifest velocity shear across the flow [e.g., 4, 11]. The interaction of the jets with the ambient plasma leads to the stratification of jets in the radial direction. A phenomenon like a limb brightening morphology in Mkn 501 revealed by VLBI radio maps indicates the radially stratified structure of jets in which a fast-moving spine is surrounded by a slow-moving sheath [e.g., 5]. Besides observational evidence, theoretical investigations propose the spine-sheath structure of jets through MHD [e.g., 6] and particle-in-cell (PiC) simulations [e.g., 7, 8]. In the case of the shear acceleration mechanism, particles are scattered on the turbulence implanted in the shear flows bearing a resemblance to the second-order Fermi-type acceleration. The observed size of synchrotron-origin X-ray structures of large-scale jets exceeds a kpc. On the other hand, the synchrotron cooling time of relativistic electrons in those jets corresponds to a maximum cooling length of sub-kpc, suggesting a need for a re-acceleration mechanism like shear acceleration. Recent Particle-in-Cell (PiC) simulations of initially unmagnetized shear flow reveal that the self-generated magnetic and electric fields are developed in SBLs via collisionless plasma instabilities, such as the Weibel instability [13], the electron counter current instability [7–9], etc that eventually lead to particle acceleration.

While the emission originating from the accretion discs of AGNs is thermal radiation, the radiation from the AGN jets is dominated by non-thermal emission comprising two distinct, broad components. The first component at lower energies from radio through to UV/X-rays results from synchrotron emission by relativistic electrons, whereas the second component extends from X-rays to gamma-rays and, in the leptonic scenario, is attributed to inverse-Compton scattering of photons emitted from the same electron population or external photons [e.g., 1]. Alternatively, the high energy peak can be explained by hadronic processes, however, their relative contribution to the higher energy component is still debatable [e.g., 3]. We consider the Compton upscattering of monoenergetic background photons by the relativistic electrons. In section 2, we discuss our simulation setup and introduce the main initial parameters of the problem. We then discuss the self-generated magnetic and electric fields from initially unmagnetized plasma and the emerging particle spectra. In section 3, we present the simulation results of radiation outputs. In section 4, we summarise the main results.

2. Simulation Setup, Self-generated Fields in SBLs, and Particle Spectra

We perform a 2D relativistic particle-in-cell simulation of relativistic SBLs considering initially unmagnetized pure electron-proton plasma using the code TRISTAN-MP [12]. The initial conditions for the simulations are shown in figure 1. In our setup, the simulation boxes have a dimension of 1024×2048 , where the number of cells along the y-axis (L_y) = $2 \times$ number of cells along the x-axis (L_x). All distances are measured in units of plasma skin depth ($c/\omega_{p,e}$), where c is the speed of light and $\omega_{p,e} = \sqrt{4\pi n e^2/m_e}$ (n , e and m_e represent

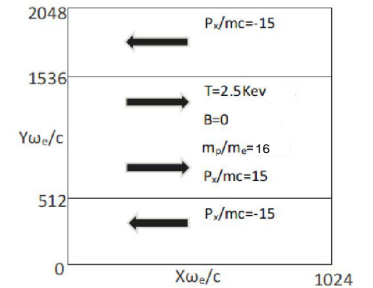


Figure 1: Simulation setup

electron number density, electronic charge, and electronic mass respectively) is the plasma frequency whereas time is measured in units of $(1/\omega_{p,e})$. The speed of light is set as $c = 0.45\Delta x/\Delta t$ to fulfill the Courant condition so that the numerical Cerenkov instability is suppressed significantly and the simulation results are physically realistic. We simulate 20 particles per cell with the proton-electron mass ratio $(m_p/m_e) = 16$ and the plasma temperature is 2.5 keV. The central 50% of the grid is occupied by the right-moving plasma called the spine and the left-moving plasma called the sheath occupies the remaining upper and lower quarters of the grid. The simulations are carried out in the equal Lorentz factor frame (ELF) with initial dimensionless momentum $(p_0) = 15$. Figures 2a and 2b show the dominant components of self-generated magnetic and electric fields, respectively. The blue and rust colors show opposite polarities. The self-generated electromagnetic fields in SBLs create turbulence in the spine-sheath interface which eventually leads to particle acceleration up to TeV energy in relativistic jets. Figure 3 shows the particle spectrum in the equal Lorentz factor frame of reference. The spectrum peaks near $\Gamma m_i/m_e$, where $\Gamma = 15$ is the bulk Lorentz factor of the counter-streaming pure electron-ion pair plasma in SBLs. We then Lorentz boost the electron momenta from the ELF to the laboratory (sheath) frame. Figure 4 represents the beam angle $(p_y/p_{x,\text{Lab}})$ vs electron Lorentz factor in the Laboratory frame (γ_{Lab}) , where p_y and $p_{x,\text{Lab}}$ are the y- and x-component of electron momenta in the ELF and the lab frame, respectively. There exists an anticorrelation between beam angles and electron energies.

3. Inverse Compton Emission Spectra

Electrons are likely to undergo radiative cooling at relativistic energies. We consider inverse Compton cooling of accelerated electrons at SBLs in a thermal blackbody external photon field of different temperatures with a characteristic frequency of $h\nu = 2.7K_B T$. The inverse Compton cooling term is calculated analytically in both cases of the Compton scattering of electrons in the angle-integrated and angle-dependent photon distribution fields. The radiation spectra are evaluated using a simple δ -function approximation for the target photon field. The radiation cooling term for the inverse Compton scattering of relativistic electrons with energies γ ($= 1/\sqrt{1-\beta^2}$) in the angle-averaged external photon field in the Thomson regime is

$$\frac{d\gamma}{dt} = \frac{\pi^4}{15} \sigma_T c K \gamma^2 \theta^4, \quad (1)$$

where $K = 8\pi/\lambda_C^3$, $\theta = K_B T/m_e c^2$, and $\sigma_T = 8\pi e^4/3m_e^2 c^4$ is the Thomson cross section. Here, λ_C , K_B , T , and e are Compton wavelength, Boltzmann's constant, radiation temperature, and electron charge respectively. The Compton wavelength λ_C can be treated as a free parameter in the simulation code. The scattered radiation due to the inverse Compton scattering of a single electron in the Thomson regime is described by the inverse Compton spectrum, peaking at the energy $\gamma^2 \epsilon$, where γ is characteristic Lorentz factor of the electron, and $\epsilon = h\nu/m_e c^2$

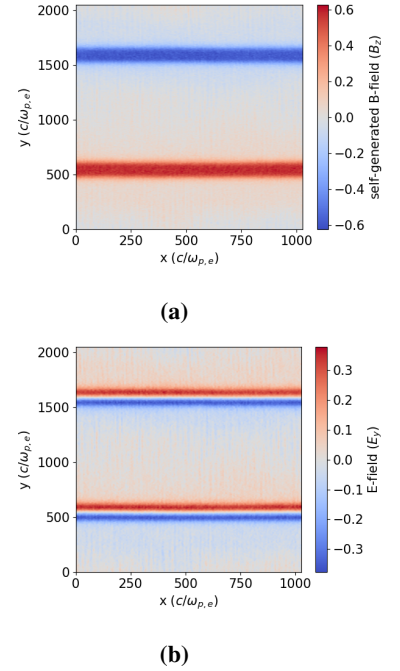


Figure 2: Self-generated (a) electric and (b) magnetic fields in SBLs obtained at a simulation time of $t = 3000/\omega_{p,e}$: blue and rust colors indicate opposite polarities.

is the unscattered photon energy. In the case of Compton scattering by ultra-relativistic electrons ($\gamma \gg 1$), all scattered photons will travel in the direction of the incoming electron [2]. Hence the Compton cross section can be approximated as $d\sigma_C/d\Omega_s d\epsilon_s = \delta(\Omega_s - \Omega_e) d\sigma_C/d\epsilon_s$, where Ω_s and Ω_e denote the directions of photons and electrons.

$$\frac{d\sigma_C}{d\Omega_s d\epsilon_s} = \frac{\pi r_e^2}{\gamma \epsilon'} \left\{ y + \frac{1}{y} - \frac{2\epsilon_s}{\gamma \epsilon' y} + \left(\frac{\epsilon_s}{\gamma \epsilon' y} \right)^2 \right\} H\left(\epsilon_s; \frac{\epsilon'}{2\gamma}, \frac{2\gamma \epsilon'}{1+2\epsilon'}\right), \quad [2] \quad (2)$$

where H is the Heaviside function that constrains the upper and lower limits of the scattered photon energies, and $y = 1 - \frac{\epsilon_s}{\gamma}$. $\epsilon' = \gamma\epsilon(1 - \beta\mu)$ is the initial photon energy in the electron's rest frame. $\mu = \cos\psi$, where ψ is the angle between the direction of propagation of the electron and photon. From equation (2), the Compton emissivity can be written as

$$j(\epsilon, \gamma, \mu) = \frac{3m_e c^3 \sigma_T \epsilon_s (1 - \beta\mu)}{8\gamma} \int_0^\infty \frac{1}{\epsilon'} \left\{ y + \frac{1}{y} - \frac{2\epsilon_s}{\gamma \epsilon' y} + \left(\frac{\epsilon_s}{\gamma \epsilon' y} \right)^2 \right\} n_{ph}(\epsilon, \theta) H\left(\epsilon_s; \frac{\epsilon'}{2\gamma}, \frac{2\gamma \epsilon'}{1+2\epsilon'}\right) d\epsilon$$

With the δ -function approximation employed for the spectral calculation, the photon density is given by $n_{ph}(\epsilon, \theta) = n_{ph}(\theta) \delta(\epsilon - 2.7\theta)$. The photon density now simplifies to $n_{ph}(\theta) = 2.4K\theta^3$. After some simplifications, the emissivity ($j(\epsilon, \gamma, \mu)$) can be integrated over the scattered photon energy within the limits constrained by the Heaviside function (H) in equation (2) to get the cooling term for inverse Compton scattering of relativistic electrons in an angle-dependent photon field in the Thomson regime as

$$\frac{d\gamma}{dt}(\mu, \gamma, \theta) = A \left[(\epsilon_{smax}^2 - \epsilon_{smin}^2) + \frac{\epsilon_{smax}^4 - \epsilon_{smin}^4}{4\gamma^2} + \frac{\epsilon_{smax}^5 - \epsilon_{smin}^5}{5\gamma^3} \right] \quad (3)$$

$$- \frac{2}{2.7\theta(1 - \beta\mu)} \left\{ \frac{(\epsilon_{smax}^3 - \epsilon_{smin}^3)}{3\gamma^2} + \frac{\epsilon_{smax}^4 - \epsilon_{smin}^4}{4\gamma^3} \right\} + \frac{1}{\gamma^4 (2.7\theta)^2 (1 - \beta\mu)^2} \left\{ \frac{\epsilon_{smax}^4 - \epsilon_{smin}^4}{4} + \frac{2(\epsilon_{smax}^5 - \epsilon_{smin}^5)}{5\gamma} + \frac{\epsilon_{smax}^6 - \epsilon_{smin}^6}{2\gamma^2} + \frac{4(\epsilon_{smax}^7 - \epsilon_{smin}^7)}{7\gamma^3} \right\},$$

where $A \equiv 0.3 c \sigma_T K \theta^2 / \gamma^2$, $\epsilon_{smax} = 5.4\gamma^2(1 - \beta\mu)\theta / (1 + 5.4\gamma\theta(1 - \beta\mu))$, $\epsilon_{smin} = 2.7\theta(1 - \beta\mu)/2$ and $\mu = \cos\psi$. ψ is the angle between directions of propagation of interacting photon and electron. Simulations are run for different radiation backgrounds from cosmic microwave background (CMB) through to ultra-violet (UV). The simulation results of the radiation outputs are shown in figures 5 and 6. In the early phases of simulations, around $t = 1500/\omega_{p,e}$ in the case of an angle-integrated photon field and around $t = 2000/\omega_{p,e}$ in the case of an angle-dependent photon

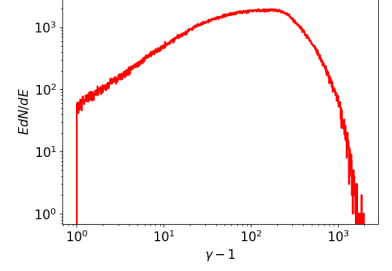


Figure 3: Electron spectrum obtained at the simulation time of $t = 3000/\omega_{p,e}$

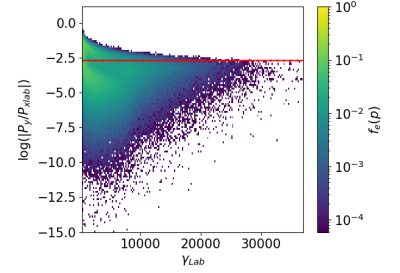


Figure 4: $p_y/p_{x,lab}$ vs γ_{Lab} : the red dashed line represents $1/\Gamma$.

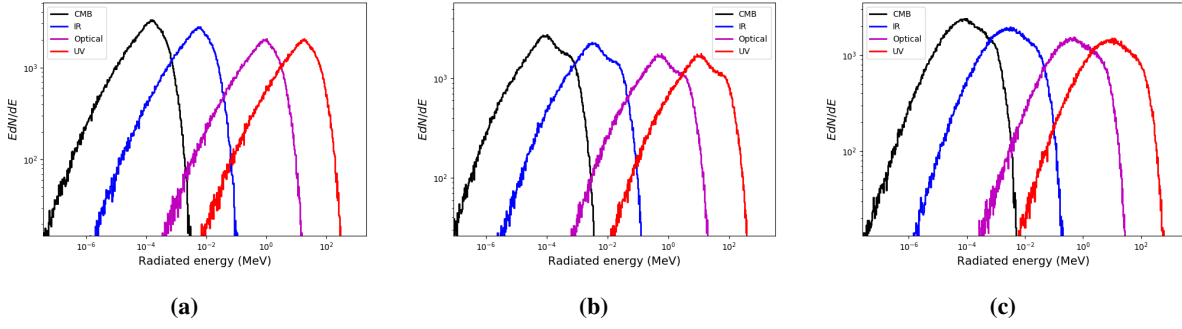


Figure 5: Radiation spectra obtained from the simulations for different radiation temperatures of the angle-independent blackbody photon field, Compton upscattered by the relativistic electrons accelerated at SBLs in relativistic jets: the spectra are obtained at different simulation times. The spectra in 5a, 5b, and 5c are plotted at $1500/\omega_{p,e}$, $2500/\omega_{p,e}$, and $3000/\omega_{p,e}$ respectively.

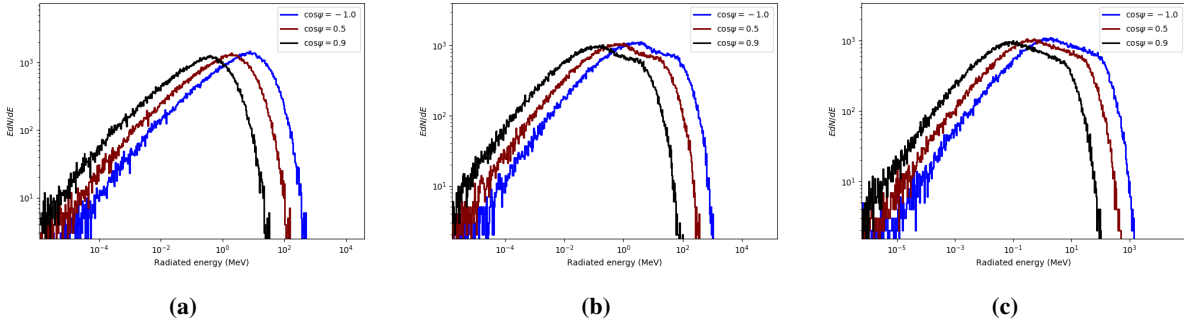


Figure 6: Inverse Compton radiation spectra for the angle-dependent UV-radiation field for different values of ψ , obtained at different simulation times: the spectra in 6a, 6b, and 6c are obtained at $2000/\omega_{p,e}$, $4000/\omega_{p,e}$, and $5000/\omega_{p,e}$ respectively. The spectra look similar for Compton scattering by relativistic electrons off blackbody photons of different temperatures.

distribution, a single component quasi-thermal inverse Compton spectrum is observed (see figures 5a and 6a). As the simulation advances, the single component spectrum develops into a double component spectrum, around $t = 2500/\omega_{p,e}$ in the former case and around $t = 4000/\omega_{p,e}$ in the latter case (see figures 5b and 6b). In the steady state of the simulations after $t = 3000/\omega_{p,e}$ and $t = 5000/\omega_{p,e}$ respectively, in both cases, the spectrum ultimately becomes a quasi-thermal

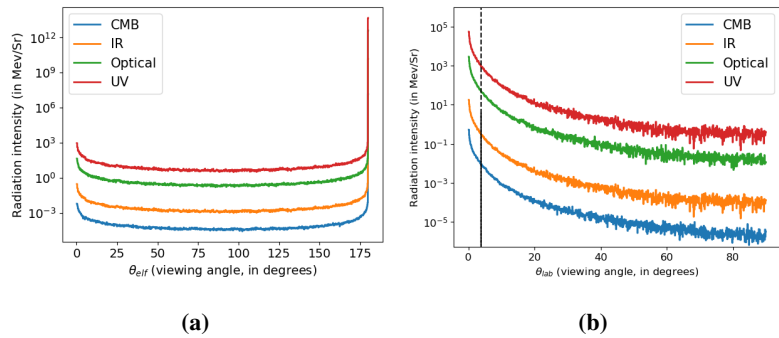


Figure 7: Radiation intensity as a function of the jet viewing angle for inverse Compton upscattered angle-averaged photons of different temperatures: figures 7a and 7b are calculated in ELF and lab frames respectively. θ_{lab} is the jet viewing angle in the lab frame.

low-frequency spectrum with a cut-off power-law tail (see figures 5c and 6c). The steady state of the simulation is achieved later in the case of inverse Compton spectra of the angle-dependent photon field, as compared to the angle-averaged photon field. We divide the total radiation energy calculated in 5 and 6 by the solid angle ($d\Omega = \sin \theta_{\text{elf}} d\theta_{\text{elf}} d\phi$) to get the radiation intensity. θ_{elf} is the angle at which the radiation from the SBL of the jet in the ELF frame is observed. Assuming the system is azimuthally symmetrical in ϕ , $d\Omega = 2\pi \sin \theta_{\text{elf}} d\theta_{\text{elf}}$. The plot of radiation intensity vs. viewing angle shows that the inverse Compton radiation emitted from the SBL of the jet is strongly boosted in the forward direction with a characteristic angle much smaller than $1/\Gamma$ indicated by the black dashed line in the figure 7b and the red line in the figure 8b.

4. Conclusion

In this paper, we study the particle acceleration at shear boundary layers in relativistic jets and the resulting radiation spectra using PiC simulations. We simulated the self-generated electric and magnetic fields in SBLs of jets from initially unmagnetized plasma. The self-consistent radiation spectra are calculated considering the inverse Compton scattering of rela-

tivistic electrons in an external photon field. The target photon field is blackbody radiation of different temperatures. Our simulation results show that efficient particle acceleration may occur in SBLs of relativistic jets. The self-generated magnetic field creates electromagnetic turbulence in jets which accelerates particles to relativistic energies. An anisotropic particle distribution arises due to plasma instabilities and the exchange of particles between the spine and sheath regions, which contributes to the radiation. In the earlier stages of simulations, both angle-integrated and angle-dependent inverse Compton radiation spectra show a single component, quasi-thermal radiation spectrum. As simulations advance, the spectrum develops into a two-component spectrum that eventually becomes a quasi-thermal low-frequency spectrum with a cut-off power-law tail. The emitted radiation is strongly boosted along the jet axis, with a characteristic opening angle of much less than $1/\Gamma$. This boosting is stronger than expected from Doppler boosting of an intrinsically isotropic radiation field in the co-moving frame of the spine. We suggest that this may resolve the long-standing problem of the Doppler factor crisis [e.g., 10].

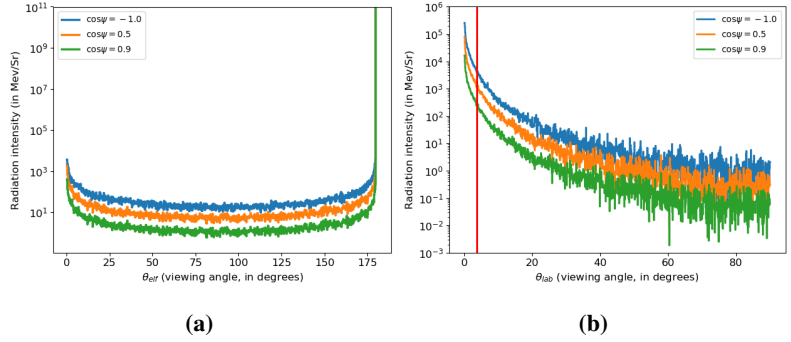


Figure 8: Radiation intensity as a function of the jet viewing angle for inverse Compton upscattered angle-dependent UV-photons with various values of ψ : figures 8a and 8b are calculated in ELF and lab frames respectively.

5. Acknowledgments

This work is supported through the South African Research Chair Initiative (SARChI) of the Department of Science and Technology and the National Research Foundation¹ (NRF) of South Africa under SARChI chair grant no. 64789.

References

- [1] Böttcher, M. 2007, *Astrophysics and Space Science*, 309,95, doi: 10.1007/s10509-007-9404-0
- [2] Boettcher, M., Harris, D.E., & Krawczynski H.: 2012, *Relativistic Jets from Active Galactic Nuclei*
- [3] Böttcher, M., Reimer, A., Sweeney, K., & Prakash, A. 2013, *ApJ*, 768, 54, doi: 10.1088/0004-637X/768/1/54
- [4] Ghisellini, G., Tavecchio, F., & Chiaberge, M. 2005, *A&A*, 432, 401, doi: 10.1051/0004-6361:2004140410.48550/arXiv.astro-ph/0406093
- [5] Giroletti, M., Giovannini, G., Feretti, L., et al. 2004, *The Astrophysical Journal*, 600, 127, doi: 10.1086/379663
- [6] Hardee, P., Mizuno, Y., & Nishikawa, K.-I. 2007, *Astrophysics and Space Science*, 311, 281, doi: 10.1007/s10509-007-9529-1
- [7] Liang, E., Boettcher, M., & Smith, I. 2013, *The Astrophysical Journal*, 766, L19, doi: 10.1088/2041-8205/766/2/L19
- [8] Liang, E., Fu, W., & Böttcher, M. 2017, *The Astrophysical Journal*, 847, 90, doi: 10.3847/1538-4357/aa8772
- [9] Liang, E., Fu, W., Böttcher, M., & Roustazadeh, P. 2018, *ApJ*, 854, 129, doi: 10.3847/1538-4357/aaa7f5
- [10] Lyutikov, M., & Lister, M. 2010, *The Astrophysical Journal*, 722, 197, doi: 10.1088/0004-637x/722/1/197
- [11] Rieger, F. M., & Duffy, P. 2022, *The Astrophysical Journal*, 933, 149, doi: 10.3847/1538-4357/ac729c
- [12] Spitkovsky, A. 2005, *AIP Conference Proceedings*, doi: 10.1063/1.2141897
- [13] Weibel, E. S. 1959, *Phys. Rev. Lett.*, 2, 83, doi: 10.1103/PhysRevLett.2.83

¹Any opinion, finding and conclusion, or recommendation expressed in this material is that of the authors, and the NRF does not accept any liability in this regard.